Turkish Journal of Electrical Engineering & Computer Sciences

http://journals.tubitak.gov.tr/elektrik/

Research Article

Turk J Elec Eng & Comp Sci
(2022) 30: 579 – 591
© TÜBİTAK
doi:10.55730/1300-0632.3799

Photonic integrated circuit-assisted optical time-domain reflectometer system

Mehmet Cengiz ONBAŞLI*
Department of Electrical and Electronics Engineering, College of Engineering, Koç University, İstanbul, Turkey

Received: 30.01.2022 • **Accepted/Published Online:** 12.01.2022 • **Final Version:** 21.03.2022

Abstract: Optical time-domain reflectometers (OTDR) are photonic systems that consist of an interrogator, a receiver and a fiber optical cable and have applications in telecommunications, security, environmental monitoring, distributed temperature and strain sensing. Since OTDR systems are bulk optical setups that consume multiple Watts of power, have large mass and volume footprint and are vulnerable to thermal drift, deployment of OTDR systems in the field is expensive, complicated and may not necessarily yield accurate sensing results. Thus, a compact, low-power, inexpensive and thermal drift-free OTDR system needs to be developed for improving the accuracy and the viability of OTDR in the field. In this study, I present the design and modeling of a photonic integrated OTDR system design based on IMEC's iSiPP50G silicon integrated photonic process design kit. The photonic integrated circuit includes a photonic modulator and a photodetector. Photonic power link budgets and the corresponding electronic signal-to-noise ratios are analyzed for 5–110 km fiber optical OTDR systems and power-efficient OTDR system designs are presented for inexpensive multiproject wafer fabrication.

Key words: Optical time-domain reflectometry, photonic integrated circuits, multiproject wafer

1. Introduction

Optical time-domain reflectometry (OTDR) is an emerging photonic probing technique with many applications in telecommunications for fiber link tests, distributed temperature, strain or biological sensing, security and environmental monitoring of structures (tunnels or bridges) for intrusion detection [1–3]. In addition to these applications, fundamental studies of fiber optical dispersion, birefringence and polarization effects [4–6], phase shift detection and nonlinear photonic effects such as pressure [7], temperature [8] or acoustically-driven [9] Brillouin, Rayleigh, Raman or optomechanical scattering light in fibers become possible with OTDR [2, 10–12]. Owing to the fundamental and applied interest in the OTDR mechanism, researchers and photonics companies have started developing OTDR systems of different types based on phase, amplitude or frequency domain reflectometry [13–16].

Figure 1 shows a simplified photonic beam path for an OTDR setup. A continuous wave laser beam at fixed wavelength (i.e. 1550 nm) is sent over a fiber optical cable. An electrooptic modulator modulates the beam as pulses between 5 and 20 kHz (chirped or regular pulsing). The pulses are sent to a circulator and then these pulses reach a multikilometer fiber optical cable. When there is a local change in the fiber's refractive index, these interrogator pulses reflect back to the circulator. The circulator reroutes the reflected pulses to the OTDR receiver, and a photodetector reads out these pulses in time domain. The local refractive index change

*Correspondence: monbasli@ku.edu.tr

This work is licensed under a Creative Commons Attribution 4.0 International License.

in the fiber may originate from a change in strain, temperature, or external dielectric constant (i.e. biosensor). The fiber length may range from a few meters to about 100 km. A series of time-domain laser pulses allow for probing the presence of reflection over the fiber and the dispersion, intensity drop or the phase shift of the reflected pulses at the receiver's photodetector could be used for detection of the signals [17].

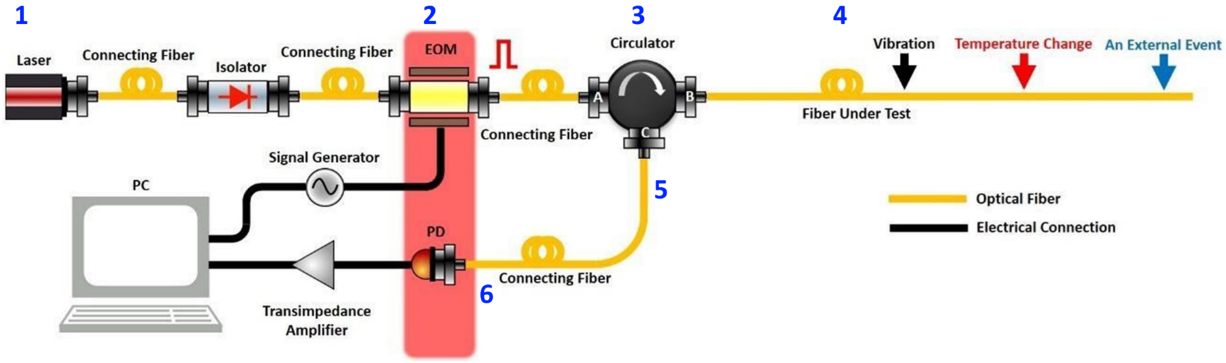

Figure 1. **Optical time-domain reflectometry (OTDR).** The laser beam (1) sent over the fiber is modulated (2) and sent through the circulator (3). A mechanical vibration or temperature change (4) modifies the local refractive index and causes reflection of the optical pulses, which are guided by the circulator (5) and detected by the receiver of the OTDR system (6). This study focuses on monolithic integration of the parts in the red box.

Previous demonstrations focused on engineering of OTDR systems to achieve an optimal point for multiple different performance metrics such as operation range, sensitivity, acquisition bandwidth and resolution [18]. In OTDR systems, a probing pulse is sent down the fiber periodically and its scattered intensity is recorded using direct photodetection [19] and heterodyne techniques [20]. In order to identify the location of the disturbance along the fiber, the time-of-flight for the probing pulse to traverse the link from the laser to the disturbance point on the fiber and to the photodiode is recorded [21]. An optical reference signal is provided by the laser to the detector or an electronic trigger is provided from a microcontroller to the photonic modulator and the analog-to-digital converter (ADC) that accompanies the photodiode and its transimpedance amplifier. The time delay between the reference and the reflected signal contains the time-of-flight information. For high spatial resolution, the photodetector response time must be as low as 100 ps so that the minimum resolvable distance can be on the order of centimeters for 10 ps pulse widths [2]. Spatial resolution, strain resolution and temperature resolution in OTDR-based fiber sensors are determined by fiber group velocity, interrogator pulse width, photodetector response time, as well as ADC delay and the factors contributing to the signal contrast (the modulation depth, photodetector responsivity, and detector noise). For achieving longer distance operation in fiber OTDR systems, the number of pulses must be reduced and the group velocity of the pulse must be high [6]. A trade-off emerges between the maximum fiber lengths that can be probed with an OTDR system and the spatial resolution. For 100 km or longer fibers, low signal-to-noise ratios (SNR $<$ 100) are common. While these SNR levels are relatively low for information transmission over telecommunication links and for their target bit error rates, OTDR sensing and anomalous event detection (intrusion, vehicle crossing, etc.) along the fiber links became feasible due to advanced signal processing, machine and deep learning methods [22–24].

Photonic integration of some of the OTDR components could reduce the cost, power consumption and footprint of the system while increasing the component density with sufficient bandwidth and operation range. Thus, on-chip integration could improve OTDR systems both in performance while reducing their costs. In this

study, I present a photonic integrated circuit design (pi-OTDR), analysis and modeling to implement a viable OTDR system with SNR $>$ 10 at the photodetector. First, the power link budget for a viable integrated OTDR system is calculated. This power link budget imposes some restrictions on the specifications of the photonic components. Next, the components are picked from IMEC's iSiPP50G component library and modelled with Lumerical Interconnect to model the overall system performance. Finally, I describe the layout design based on photonic packaging constraints.

2. Design of the pi-OTDR chip

The proposed photonic integrated circuit (PIC) design of the pi-OTDR consists of an interrogator section (a fiber Bragg grating in-coupler, electrooptic modulator and fiber Bragg grating out-coupler) and a receiver section (a fiber Bragg grating in-coupler, a waveguide-integrated Germanium photodetector). Since the integration of laser, optical isolator, and the circulator is technically challenging and not commercially available by foundries for multiproject wafer fabrication, these three components are going to be externally connected to the PIC. A 1552.48 nm continuous wave (CW) laser emits light to the optical isolator and couples into the interrogator end of the pi-OTDR PIC chip using a fiber Bragg grating coupler (FBG). The CW beam is then amplitude-modulated using an integrated electrooptic (EO) modulator and the pulses are transmitted into port A of the circulator using a FBG. The circulator routes the pulses to the fiber under test (FUT) connected to the port B of the circulator. When a mechanical vibration or temperature drift changes the local refractive index along the fiber under test, the laser pulse reflects back to the circulator. The reflected pulse is routed by the circulator into Port C, which is connected to the receiving block of the pi-OTDR through another FBG. The reverse biased waveguide-integrated Germanium photodetector converts the optical pulse to photocurrent which is processed in the electronics.

The PIC design must include EO modulators with sufficiently high modulation depth and low insertion loss and photodiodes with high responsivity, low dark current and sufficient bandwidth. A power link budget analysis in Table 1 indicates the component losses as well as the key specifications that are necessary for the integrated pi-OTDR operation. The 40 mW 1550 nm CW laser is a bulk component that has –29 dBm side modes, which determines the noise limit in the optical power. This limit also determines the ACTIVE LOW optical power level for a direct detection with ON-OFF keying of optical pulses. Hence, the side mode suppression ratio (45 dB) is taken as the upper limit for electrooptic modulation. As this CW beam passes through the isolator and the FBG, it accumulates 0.7 and 5.428 dB losses, respectively (based on the specifications of the suggested parts). By the time the signal reaches the modulator, the losses accumulate and the optical input can range from –0.898 dBm down to –29 dBm power. To achieve the highest signal contrast in electrooptic modulation, modulator architecture must be determined to yield modulation depths near or higher than the difference between the minimum and the maximum signals, 28 dB. After adding all the possible losses listed in Table 1, the total maximum power with EDFA is about 9.246 dBm. In reality, OTDR signals have a reflection factor of less than 0.1, meaning the input power intensity to the photodiode could be at least 10 dB lower. As a result, the laser input essentially determines the 28 dB optical ON/OFF signal contrast before photodetection.

To span this power budget as optimally as possible, an electrooptic modulator must be chosen with a modulation depth close to 28 dB near 1550 nm operation wavelength. Two Si CMOS-compatible electrooptic modulator designs are available for MPW designs based on IMEC's iSiPP50G MPW device library: (1) ring and (2) Mach–Zehnder modulators. Ring modulators have a small footprint ($20 \times 10\ \mu m^2$), but their modulation is about 11.36 dB near 1544.4 nm center wavelength for –2V modulation voltage with 12 dB insertion loss. These

Table 1. Power link budget for the integrated pi-OTDR circuit. The components are ordered along the beam path. EDFA, FBG, PDK stand for erbium-doped fiber amplifier, fiber Bragg grating coupler and process design kit, respectively. An external EDFA might be added between the EOM and the circulator in Figure 1 to extend the range of the pi-OTDR system. Components are labeled as external (E) or integrated (I).

Component name (E: external, I: integrated)	Power contribution (dBm or dB)	Optical power range after the component (max, min) (dBm)	Maximum allowed optical input power (dBm) for the component	Noise contribution (dBm or dB)	Suggested part name
(1) Laser (E)	16 dBm (40 mW)	(16, –29)	-	-29 dBm (side mode suppression ratio: 45 dB)	Thorlabs SFL1550S
(2) Isolator (E)	–0.7 dB	(15.3, –29)	24.7	-	Thorlabs IO-H-1550
(3) FBG (I)	–5.428 dB	(9.872, –29)	10		IMEC iSiPP50G PDK
(4) Mach–Zehnder Modulator (I)	–10.77 dB (insertion loss)	(–0.898, –29)	10	–40.898 dBm (for min. 40 dB modulation depth)	IMEC iSiPP50G PDK
(5) FBG (I)	–5.428 dB	(–6.326, –29)	10		IMEC iSiPP50G PDK
(6) EDFA (E)	30 dB	(23.674, –29) (with EDFA) (–6.326, –29) (w/o EDFA)	10	4 dB	Thorlabs EDFA100S
(7) Circulator (E)	–1 dB	(22.674, –29) (with EDFA) (–7.326, –29) w/o EDFA)	27		Thorlabs 6015-3
(8) Fiber under test (E) (propagation loss)	–0.2 dB/km * 2d d: distance	(22.674 – 0.4d, –29) (with EDFA) (–7.326 – 0.4d, –29) (max, w/o EDFA)	30+		
(9) FBG (I)	–5.428 dB	(17.246 – 0.4d, –29) (with EDFA) (–12.754 – 0.4d, –29) (w/o EDFA)	10		IMEC iSiPP50G PDK
Total max. power at the photodetector (20 km)		(9.246, –29) (with EDFA) (–20.754, –29) (w/o EDFA)	< 10		

characteristics are not sufficient for optimal signal contrast in OTDR. Mach–Zehnder modulators (MZM), in contrast, have more than 40 dB (47 dB) modulation depth for –3V modulation voltage and wider bandwidth operation than ring modulators. MZM's have two disadvantages though, which are 10.77 dB insertion loss and large footprint (1.5×1 mm^2). Figure 2 shows the transmission spectra for the MZM at 0 V and –3V near 1552.48 nm obtained from the Lumerical Interconnect calculations using IMEC's PDK in part (a) and heater tuning of the spectra in part (b). A key advantage of MZM is that an integrated heater allows for dynamic tuning of the MZM transmission dip wavelength by thermooptic phase shifting for exactly matching the laser wavelength. The heater contacts are additional pads that provide thermally-driven refractive index change with

voltage from 0V to 2V. The transmission dip can be changed as much as 0.2 nm with 2V heater voltage. Hence, MZM is used for the integrated EO modulator device architecture in the pi-OTDR design.

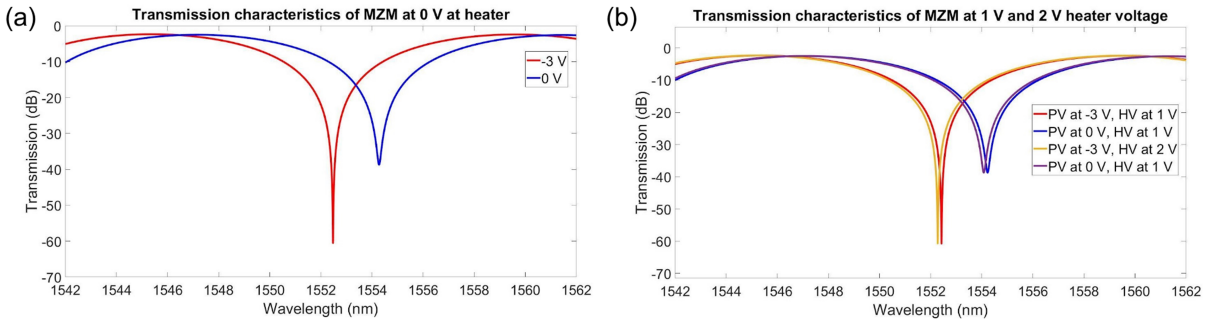

Figure 2. **Mach–Zehnder modulator (MZM) transmission characteristics.** a) Simulated MZM transmission spectra at 0 and –3 V at modulating input (0 V at heater voltage). 47 dB modulation depth can be achieved at 1552.48 nm. (b) Simulated MZM transmission characteristics at 0 and –3 V phase voltage (PV), at 1 V and 2 V heater voltage (HV). The simulation results are based on IMEC's experimental iSiPP50G PDK data.

Table 1 indicates that the ultimate SNR will be determined by fiber length, insertion losses added by the components and the noise equivalent power of the integrated photodetector. An optimal OTDR system would achieve the highest SNR for the longest length of fiber under test. Thus, thermal and vibration sensing can extend over longer distances. Since the propagation loss of fibers diminishes the optical power with distance, SNR decreases with longer fibers. Hence, we define a figure of merit of F = SNR × distance, which is the product of the fiber length and the SNR at the photodetector. The SNR of the photodetector is defined as the difference between the optical power received (in dBm) and the noise equivalent power (NEP, in $W/\sqrt{Hz}$). Here, we take the noise threshold as –35 dBm, which is actually higher than most of the noise thresholds of the integrated germanium photodetectors in IMEC's iSiPP50G PDK. The photodetectors in IMEC's PDK have noise thresholds ranging from –34 dBm to –51 dBm depending on the load resistance and diode capacitances. Hence, our SNR estimates target the system performance when the worst photodetector performance is achieved.

Figure 3 shows the SNR and SNR × distance product curves as a function of fiber length for the OTDR systems with EDFA and without EDFA in parts (a) and (b), respectively. In both cases, there is an optimal fiber distance (65 km for part a, 28 km for part b) which maximizes the figure of merit for optimal SNR and fiber length. When there is an EDFA between the pi-OTDR chip and the circulator, the beam can propagate for 37 km further from the chip without EDFA. Hence, the use of an EDFA is suggested for the overall system while keeping high SNR and the optical power does not exceed the allowed limits for the chip at any point.

The photodetector choice in our pi-OTDR system must have high responsivity (R > 0.8 A/W) around 1550 nm, low dark current (< 20 nA), small footprint and low reverse bias requirements. Although the details of the photodetector choice cannot be fully disclosed due to confidentiality requirements of IMEC's iSiPP50G component library, our choice of waveguide-integrated germanium photodetector satisfies each of these requirements at –1V reverse bias with around 10 nA dark current noise threshold = dark current × reverse bias voltage; ranging -50 to -37 dBm), and 1 A/W responsivity. The photodiode has bandwidth exceeding 20 GHz around 1550 nm operation wavelength.

Other design constraints based on passive integrated components include the waveguide losses and the FBG coupling losses. –5.428 dB FBG coupling loss (Table 1) is a fixed attenuation obtained from modeling the

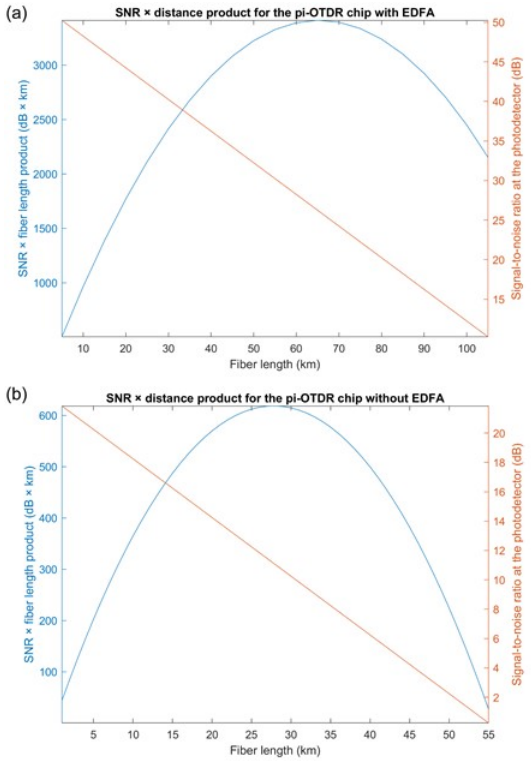

Figure 3. **SNR and SNR x distance product curve.** Optimal SNR × distance product conditions with EDFA (65 km, SNR = 26.2 dB) and without EDFA (28 km, SNR = 11.0 dB) show that fiber length can be maximized while keeping sufficiently high SNR ($>$ 10 dB) for both cases.

FBG of IMEC's iSiPP50G PDK around our operation wavelength in the Lumerical Interconnect. The reported FBG insertion loss refers to the specific coupling scheme of the set-up and may differ from an optimum coupling scheme of this component. The integrated single mode waveguide loss is around 1.36 dB/cm, which is lower than the error margin for the losses of other components.

While the proposed photonic integrated circuit is not a finished product, these integrated circuits could help reduce the total mass, the system dimensions and the total power consumption with respect to a commercial bulk OTDR system. A commercial telecom-style OTDR tool can have a mass of about 1.8 kg, dimensions of about 25 cm (W) × 18 cm (H) × 55 mm (D), and power consumption of about 10 W. The mass of the integrated OTDR system can be reduced to below 1000 g, where mass savings might come from eliminating the bulk electric cabling, the packaging case and the cooling units for the photodetector and modulator. The integrated OTDR system can be fit in a box of 80 mm (W) × 80 mm (L) × 20 mm (H), in which the photonic integrated circuit takes 25 mm (W) × 25 mm (L) × 0.5 mm (H); the external laser takes 55 mm (W) × 30 mm (L) × 10 mm (H), the isolator takes less than 50 mm in length and the readout electronics board could be within 80 mm (W) × 80 mm (L) × 6 mm (H). These dimensions are based on Thorlabs's SFL1550S laser and IO-H-1550 optical isolator datasheets. Therefore, one may estimate a reduction of more than an order of magnitude in total volume (from 25cm (W) × 18 cm (H) × 55 mm (D) to 80 mm (W) × 80 mm (L) × 20 mm (H)). The total power consumption of the integrated OTDR system can be reduced to below 1 W, since the sum of the power consumptions of the laser (40 mW), the modulator ($<$ 2 mW, per IMEC's iSiPP50G library handbook), the photodetector ($<$ 1

μW), the modulator driver circuit ($<$ 500 mW) and the readout electronics (analog-to-digital converter behind the Ge waveguide photodetector) ($<$ 500 mW) might not exceed 1 W. Therefore, even with the peripheral electronics, one may estimate less than about 1 W power consumption in the integrated OTDR system. Thus, at least an order of magnitude improvement in the total power consumption might be expected.

3. Analysis of the integrated OTDR system

The system has been modeled using Lumerical Interconnect and IMEC's iSiPP50G with the configuration shown in Figure 4. In this configuration, 1552.48 nm narrow linewidth CW laser has been used with a short fiber and the blue box shows our photonic integrated OTDR circuit. The connectors on the integrated chip are the FBG units. The photodiode is reverse biased under 2V (–2V bias, no additional AC small-signal bias) and the modulator is also biased at –2V for the intended phase shift.

Figure 5 shows the simulated photocurrent for a periodic interrogator pulse stream over 5 ns and the change of the peak photocurrent magnitude as a function of fiber length. Here, not EDFA was used. The photocurrent output diminishes with increasing fiber length due to the exponential power decay. Our model results indicate that the fiber optical losses determine the photocurrent. For 0 km (no fiber), 30 km, and 60 km, the optical powers at the photodiode are –12.754, –24.754, and –36.754 dBm, respectively. Since the noise threshold is estimated around –29 dBm, the SNR's for the 0, 30, and 60 km cases are 16.2, 4.246 and below the noise threshold, respectively. The bit stream in Figure 5a falls below the noise threshold and cannot be detected.

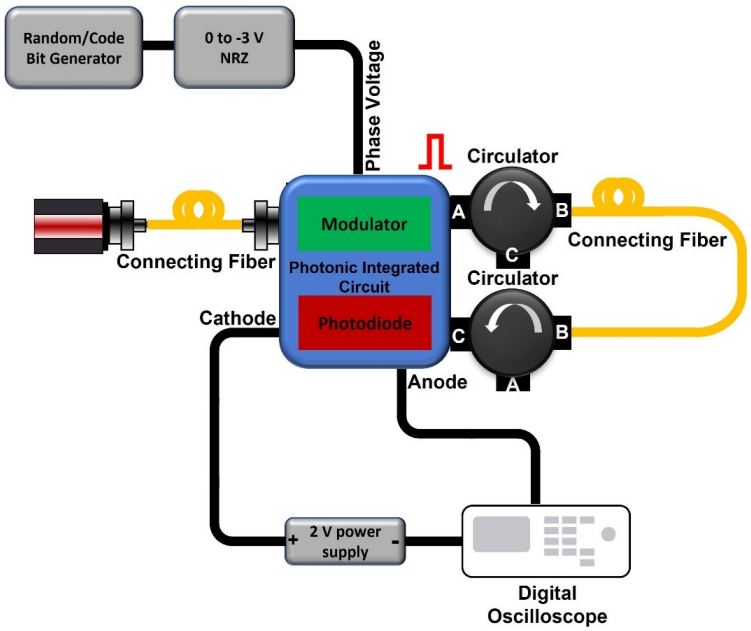

Figure 4. Test configuration for pi-OTDR chip and its peripheral optics and electronics. The electronics includes a random bit generator, a voltage pulse generator with 0 to –2V nonreturn-to-zero (NRZ) bias scheme and a DC power supply for reverse biasing the photodiode. The PIC transceiver module has been modeling for the operation wavelength of 1552.48 nm by modeling in Lumerical Interconnect software and using IMEC iSiPP50G PDK.

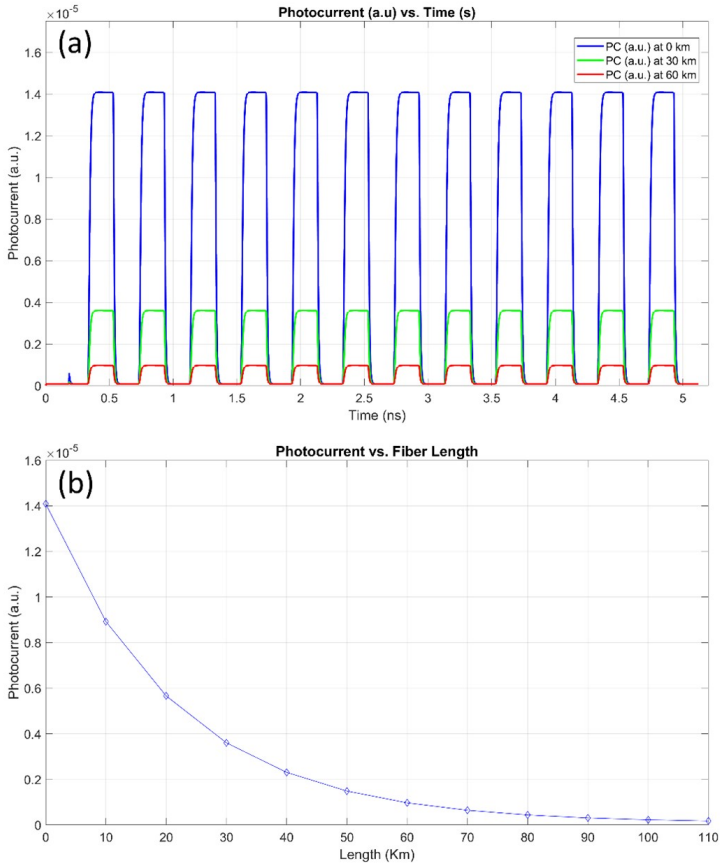

Figure 5. **Simulated photocurrent of the pi-OTDR circuit over time for different fiber lengths.** The test configuration shown in Figure 4 has been used for modeling the pi-OTDR chip. (a) Time-domain photocurrent magnitude diminishes for fibers of increasing lengths (0, 30, and 60 km). Optical losses rather than dispersion dominate the time-domain photocurrent output. (b) Photocurrent output for increasing fiber lengths shows negligible photodiode output for fibers longer than 50 km. The operation wavelength is 1552.48 nm.

4. pi-OTDR chip layout and electronic and optical packaging constraints

Our Pi-OTDR chip layout must be designed by taking the photonic packaging constraints into account, since the component areas, the FBG and fiber optical cable interfaces and the electric contact pads each have significant floor spacing requirements that may significantly increase fabrication costs. These requirements are based on Tyndall National Institute's Advanced Photonics Packaging and System Integration Guidelines as part of Europractice [25], but packaging requirements from other institutions would be similar unless automated photonic packaging technologies are developed. Other photonic packaging services may impose different requirements depending on voltage ranges and contact pad dimensions, heat extraction conditions, external package dimensions, microelectronic integration with wire bonding and silicon interposers, FBG geometry as well as the fiber epoxy technology.

Based on Tyndall's contact pad and FBG spacing requirements, chip areas larger than the functional component areas might have to be reserved for packaging. I first start this section by presenting the packaging requirements of Tyndall National Institute that we consider to fit all the components in the available floor plan of 2500×2500 µm^2 (quarter block in IMEC's MPW runs). The first requirement is that all the FBGs should

have a minimum distance of 750 µm from the top, left and bottom edges and should be spaced 127 µm apart. Second, an exclusion region of a minimum of 500 µm is mandatory for mechanical epoxy bonding of the fiber to the FBG and no other photonic or electrical component can be placed in this exclusion region. Third, the bondpads and the FBGs should not be on the opposite edges but must occupy orthogonal edges. Fourth, the electric bond pads must be at a minimum of 50 µm and at a maximum of 500 µm away from the edge of the chip. The spacing between two consecutive electric bond pads should be a minimum of 150 µm and all of the bond pads must be exactly aligned with each other. All the mentioned packaging requirements are shown in Figure 6.

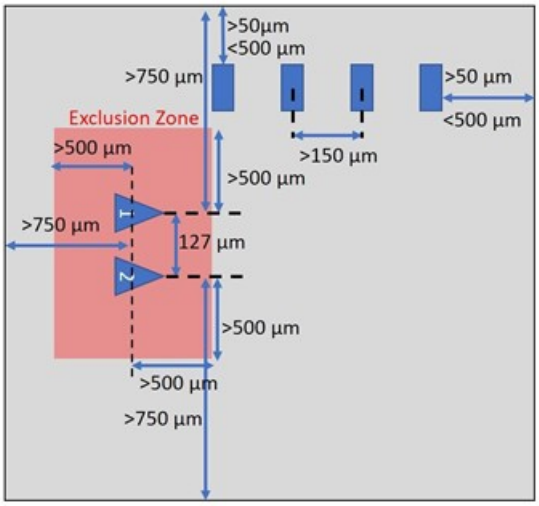

Figure 6. **Packaging requirements of Pi-OTDR 2500 × 2500 µm^2 chip.** FBGs should have a minimum distance of 750 µm from the edges of the chip and the spacing between the FBGs should be 127 µm. An exclusion zone (red) of 500 µm on all four sides of FBGs is mandatory for mechanical and optical epoxy bonding of fibers to the FBGs and no optical or electrical component should be placed in this exclusion zone. The bond pads must all be aligned with each other and must be spaced a minimum distance of 50 µm and a maximum distance of 500 µm from the edges of the chip. The bond pads must be 150 µm apart from each other at minimum.

Figure 7(a) shows the layout for the 2500 × 2500 µm^2 pi-OTDR chip after taking photonic packaging constraints into account. The chip contains FBGs for inputs and outputs, one photodiode, one MZM and nine bond pads (BP). Six FBGs spaced at 127 µm apart, a zoomed in version of them is shown in Figure 7b, the top and bottom FBGs are connected directly by a single mode strip waveguide (SM-SW) as shunt for alignment of fiber array. The input of the MZM is connected to the second from top FBG with a SM-SW. The output from the MZM is routed via SM-SW to the third FBG. The fourth and the fifth FBGs are connected to the inputs of the waveguide integrated germanium PD which is shown in Figure 7c. A summarized FBG connection is shown in Table 2.

Meeting all these requirements with inline fiber input (left-hand side) and fiber output (right-hand side of the chip) was not possible within the 2500 × 2500 µm^2 chip area. We solved this issue by choosing a 10-channel (2-shunt and 8 user channels) fiber array that connects all inputs and outputs to the chip from only one edge. For aligning the fiber, 2 extra grating couplers were added as a shunt. The active components with bond pads and wires (MZM and PD) are placed far away from the exclusion zone. As the existing bond pads on the MZM did not meet the minimum spacing requirements of the packaging, we placed seven bond pads spaced at 160

µm and routed them to the electrical connections of MZM. Two more inline bond pads were added for electrical connections of the waveguide integrated germanium PD for biasing and photodetection. The nine bond pads spaced at 100 µm at the top of the pi-OTDR chip are connected to the electrical inputs and outputs of the MZM and the PD has been used for biasing, signal input for modulation, and receiving the photocurrent. Table 3 shows the details of the connections 1–9 (bond pads, left to right). The bond pads are shown in Figure 7d.

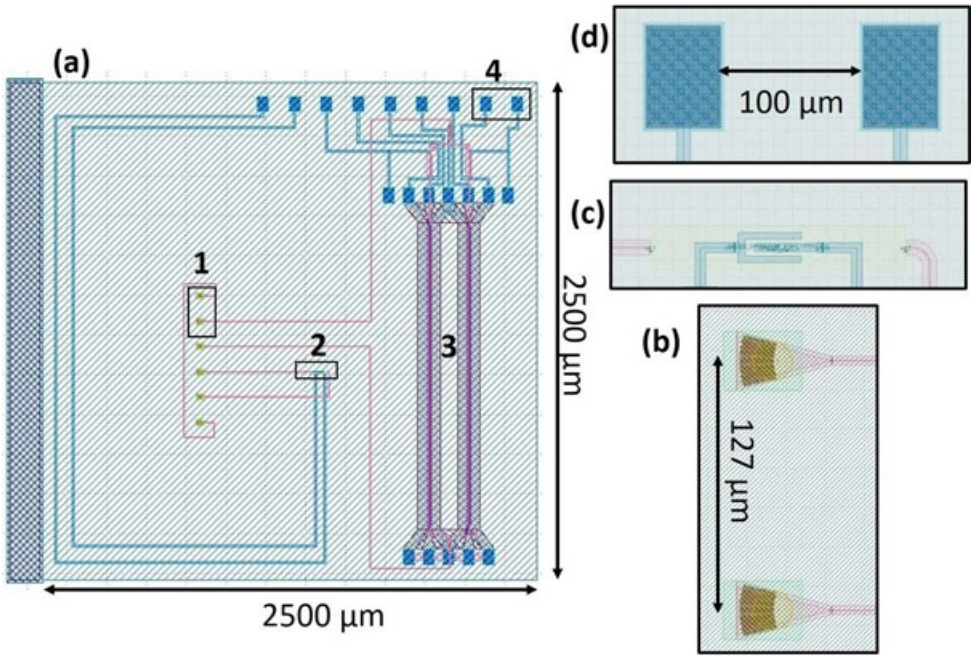

Figure 7. Pi-OTDR chip layout (2500 × 2500 µm^2). (a) The pi-OTDR chip layout has four main components: (1) six FBGs, (2) waveguide-integrated germanium photodetector, (3) an MZM, (4) nine electrical bond pads. The closer views of the component footprints for the (b) FBGs (must have 127 µm spacings due to packaging constraints), (c) the waveguide integrated germanium photodetector, (d) the electric bond pads with 100 µm spacings. The FBGs in (b) are the etched structures on the chip (not the fiber), typically have 220 nm silicon thickness, 70 nm etch depth, 20° incident angle, $n_{cladding} = 1.44$, transverse electric (TE) polarization, 500 nm waveguide width, 1550 nm center wavelength [26].

Table 2. Optical connections description to fiber Bragg grating couplers, numbered from top to bottom.

Fiber no.	Description	Notes
1	Shunt	Not connected
2	Input to modulator	Input from the laser (max 10 dBm)
3	Output from modulator	Output to network/circulator
4	Input 1 to photodiode	Input from the network/circulator
5	Input 2 to photodiode	Not connected
6	Shunt	Not connected

5. Conclusion

This study shows that photonic integration of OTDR interrogator and receiver modules might be feasible and advantageous based on the reduction of modulator and photodetector footprint and power consumption while

Table 3. Electrical connections description to the bond pads, numbered from left to right.

Pin number	Description	Notes
1	Photodiode anode	Bias at –2V photocurrent output
2	Photodiode cathode	0 V (ground)
3	Heater 2 input	0 V (ground) Typical
4	Ground	0 V (ground)
5	Signal 2	0 V (ground)
6	Ground	0 V (ground)
7	Signal 1	Not connected
8	Ground	0 V (ground)
9	Heater 1	0 V (ground)

keeping their bandwidth high ($>$ 40 GHz). The power link budget analysis shows that high modulation depth (28 dB or higher) is needed for efficient use of the power budget and high SNR at the photodetector. In addition, an integrated photodetector architecture with low noise thresholds ($<$ –29 dBm) and high responsivity (0.8 A/W or higher) is necessary for low power consumption, high SNR and precise event classification after preprocessing OTDR signals. Overall, the constraints guided the design to germanium waveguide-integrated photodetector with low dark current and high responsivity and to MZM with high modulation depth. The MZM's heater contacts allow for dynamic tuning of the transmission dip to match the exact operation wavelength.

The photonic integrated circuit modeling and modeling in Lumerical Interconnect showed that the propagation loss in the fiber and the component insertion losses could be the main factors which need to be minimized for high SNR at the photodetector and the long fiber distance. The power link budget and the Lumerical Interconnect models show that a trade-off emerges between the SNR at the photodetector and the fiber length of the OTDR system. The maximum distance with the highest SNR is estimated to be 65 km and 30 km for circuits with and without EDFA, respectively. Hence, periodic interrogation of the OTDR system could yield the highest SNR for the longest fiber distance under these conditions.

Along with component characteristics, power link budget and OTDR operation requirements, photonic and electronic packaging constraints impose circuit layout restrictions on the chip floor planning. As optical fibers are mounted and bonded mechanically and optically to the FBG with more than 1 mm exclusion zone, fiber connections have been assembled on one side (instead of two sides) of the chip to save chip space. All constraints including photonic design rules, packaging restrictions and functional requirements must be factored into the chip designs before submitting layouts for photonic MPW tapeout. The pi-OTDR design presented here is currently being fabricated as a multiproject wafer chip, and is going to be packaged and tested at Tyndall National Institute. The PIC design and modeling flow presented here in detail could pave the way for other application-specific photonic integrated circuits layouts with low power consumption, small footprint, wide bandwidth, CMOS compatibility and could allow for electronic-photonic multichip packaging and photonic interposers for ultrawide bandwidth applications.

References

[1] Bai Q, Wang Q, Wang D, Wang Y, Gao Y et al. Recent Advances in Brillouin Optical Time Domain Reflectometry. Sensors 2019; 19: 1862. doi:10.3390/s19081862

[2] Rogers AJ. Polarization-optical time domain reflectometry: a technique for the measurement of field distributions. Applied Optics 1981; 20: 1060-1074. doi:10.1364/AO.20.001060

[3] Aoyama K, Nakagawa K, Itoh T. Optical time domain reflectometry in a single-mode fiber. IEEE Journal of Quantum Electronics 1981; 17: 862-868. doi:10.1109/jqe.1981.1071237

[4] Husdi IR, Nakamura K, Ueha S. Sensing characteristics of plastic optical fibres measured by optical time-domain reflectometry. Measurement Science and Technology 2004; 15: 1553-1559. doi:10.1088/0957-0233/15/8/022

[5] Ross JN. Birefringence measurement in optical fibers by polarization-optical time-domain reflectometry. Applied Optics 1982; 21: 3489-3495. doi:10.1364/AO.21.003489

[6] Rogers AJ. Polarization-Optical Time Domain Reflectometry. Proceedings of SPIE 1981; 0236: 358-364.doi:10.1117/12.959037

[7] Mikhailov S, Zhang L, Geernaert T, Berghmans F, Thévenaz L. Distributed Hydrostatic Pressure Measurement Using Phase-OTDR in a Highly Birefringent Photonic Crystal Fiber. Journal of Lightwave Technology 2019; 37: 4496-4500.

[8] Bolognini G, Park J, Soto MA, Park N, Di Pasquale F. Analysis of distributed temperature sensing based on Raman scattering using OTDR coding and discrete Raman amplification. Measurement Science and Technology 2007; 18: 3211-3218. doi:10.1088/0957-0233/18/10/s24

[9] Wang Z, Zhang B, Xiong J, Fu Y, Lin S et al. Distributed Acoustic Sensing Based on Pulse-Coding Phase-Sensitive OTDR. IEEE Internet of Things Journal 2019; 6: 6117-6124. doi:10.1109/jiot.2018.2869474

[10] Horiguchi T, Shimizu K, Kurashima T, Tateda M, Koyamada Y. Development of a distributed sensing technique using Brillouin scattering. Journal of Lightwave Technology 1995; 13: 1296-1302. doi:10.1109/50.400684

[11] Park J, Bolognini G, Lee D, Kim P, Cho P et al. Raman-based distributed temperature sensor with simplex coding and link optimization. IEEE Photonics Technology Letters 2006; 18: 1879-1881, doi:10.1109/lpt.2006.881239

[12] Bashan G, Diamandi HH, London Y, Preter E, Zadok A. Optomechanical time-domain reflectometry. Nature Communications 2018; 9: 2991. doi:10.1038/s41467-018-05404-0

[13] Lu Y, Zhu T, Chen L, Bao X. Distributed Vibration Sensor Based on Coherent Detection of Phase-OTDR. Journal of Lightwave Technology 2010; 28: 3243-3249.

[14] Von Der Weid JP, Passy R, Mussi G, Gisin N. On the characterization of optical fiber network components with optical frequency domain reflectometry. Journal of Lightwave Technology 1997; 15: 1131-1141. doi:10.1109/50.59695

[15] Wang Z, Zhang L, Wang S, Xue N, Peng F et al. Coherent Φ-OTDR based on I/Q demodulation and homodyne detection. Optics Express 2016; 24: 853-858. doi:10.1364/OE.24.000853

[16] Murray MJ, Redding B. Quantitative amplitude-measuring Φ-OTDR with $\mathrm{p}\epsilon/\sqrt{Hz}$ sensitivity using a multi-frequency pulse train. Optics Letters 2020; 45: 5226-5229. doi:10.1364/OL.400159

[17] Fernández-Ruiz MR, Costa L, Martins HF. Distributed Acoustic Sensing Using Chirped-Pulse Phase-Sensitive OTDR Technology. Sensors 2019; 19: 4368. doi:10.3390/s19204368

[18] Soriano-Amat M, Martins HF, Durán V, Costa L, Martin-Lopez S et al. Time-expanded phase-sensitive optical time-domain reflectometry. Light: Science & Applications 2021; 10: 51. doi:10.1038/s41377-021-00490-0

[19] Muanenda Y, Oton C, Faralli S, Di Pasquale F. High performance distributed acoustic sensor using cyclic pulse coding in a direct detection coherent-OTDR. Proceedings of SPIE 2015; 9655: 965547. doi:10.1117/12.2203103

[20] Liu H, Pang F, Lv L, Mei X, Song Y et al. True Phase Measurement of Distributed Vibration Sensors Based on Heterodyne φ-OTDR. IEEE Photonics Journal 2018; 10: 1-9. doi:10.1109/jphot.2018.2791101

[21] He H, Shao L, Luo B, Li Z, Zou X et al. Multiple vibrations measurement using phase-sensitive OTDR merged with Mach-Zehnder interferometer based on frequency division multiplexing. Optics Express 2016; 24: 4842-4855. doi:10.1364/OE.24.004842

[22] Wang Z, Lou S, Liang S, Sheng X. Multi-Class Disturbance Events Recognition Based on EMD and XGBoost in ϕ-OTDR. IEEE Access 2020; 8: 63551-63558. doi:10.1109/access.2020.2984022

[23] Shi Y, Wang Y, Wang L, Zhao L, Fan Z. Multi-event classification for Φ-OTDR distributed optical fiber sensing system using deep learning and support vector machine. Optik 2020; 221: 165373. doi:10.1016/j.ijleo.2020.165373

[24] Tejedor J, Macias-Guarasa J, Martins HF, Pastor-Graells J, Corredera P et al. Machine Learning Methods for Pipeline Surveillance Systems Based on Distributed Acoustic Sensing: A Review. Applied Sciences 2017; 7: 841. doi:10.3390/app7080841

[25] Selim R. (2021, May 2019). Advanced Photonics Packaging and System Integration Services within EUROPRACTICE. 1.5. Retrieved from https://europractice-ic.com/wp-content/uploads/2019/05/Tyndall_Photonics_Packaging_within_EuroPractice_V1.5.pdf

[26] Wang Y, Flueckiger J, Lin C, Chrostowski L. Universal grating coupler design. Proceedings of SPIE 2013; 8915: 284-290. doi:10.1117/12.2042185